Experimental Calibration of Heat Transfer and Thermal Losses in a Shell-and-Tube Heat Exchanger

Javier Bonilla[1,2] Alberto de la Calle[1,2] Margarita M. Rodríguez-García[1]
Lidia Roca[1,2] Loreto Valenzuela[1]

[1]CIEMAT-PSA, Centro de Investigaciones Energéticas, Medioambientales y Tecnológicas - Plataforma Solar de Almería, Spain, {javier.bonilla, alberto.calle, margarita.rodriguez, lidia.roca, loreto.valenzuela}@psa.es
[2]CIESOL, Solar Energy Research Center, Joint Institute University of Almería - CIEMAT, Almería, Spain

Abstract

Many commercial solar thermal power plants rely on thermal storage systems in order to provide a stable and reliable power supply. The heat exchanger control strategies, to charge and discharge the thermal storage system, strongly affect the performance of the power plant. With the aim of developing advanced control strategies, a dynamic model of a shell-and-tube heat exchanger is being developed. This heat exchanger belongs to the CIEMAT-PSA molten salt testing facility. The goal of this facility is to study thermal storage systems in solar thermal power plants. During experimental campaigns performance losses with respect to design performance were noticed in the heat exchanger. Therefore and in order to develop an accurate heat exchanger model, thermal losses as well as heat transfer correlations on both fluid sides have been calibrated against experimental data.
Keywords: calibration, heat exchanger, heat transfer correlation, thermal losses, JModelica.org

1 Introduction

Many factors such as, environmental issues, concern about sustainability and rising cost of fossil fuels are presently encouraging research and investment into renewable resources. Renewable energy power plants face the main problem of dispatchability of demand due to the variability of their power sources. Nevertheless, solar thermal power plants are appropriate for large-scale energy production since they efficiently store heat in Thermal Energy Storage (TES) systems. Thus, many commercial solar thermal power plants rely on this technology (Herrmann and Kearney, 2002).

The performance of solar thermal power plants with TES systems is highly influenced by the heat exchanger control strategies applied in the charging and discharging processes (Zaversky et al., 2013). Therefore, advanced control strategies may improve the performance of the whole plant. For this reason, a dynamic heat exchanger model is being developed. This heat exchanger is part of the CIEMAT-PSA molten salt testing facility. This multipurpose molten salt testing facility is devoted to evaluate and control the heat exchange between molten salt and different kind of heat transfer fluids which could be used in solar thermal power plants.

During experimental campaigns, performance losses were noticed in the heat exchanger with respect to design performance. A dynamic heat exchanger model is being developed in order to evaluate such losses (Bonilla et al., 2015). This paper shows the followed procedure to calibrate heat exchanger thermal losses as well as heat transfer correlations for both fluid sides.

The paper is organized as follows, section 2 briefly describes the experimental plant and the heat exchanger. Section 3 carries out an analysis of heat transfer in the heat exchanger. Once this analysis is completed, heat transfer correlations in the literature are examined in section 4, thermal losses are estimated against experimental data in section 5 and heat transfer coefficients are also estimated by means of calibrating heat transfer correlations in section 6. Finally, main conclusions together with ongoing work tasks are presented in section 7.

2 Experimental Plant

A multipurpose molten salt testing facility, with the goal of studying TES system, was set up at Plataforma Solar de Almería (PSA), division of CIEMAT, the public research center for Energy, Environmental and Technological Research, which is owned by the Spanish government. The CIEMAT-PSA molten salt testing facility can evaluate and control the heat exchange between molten salts and potential heat transfer fluid for solar thermal power plants, i.e. thermal oil and pressurized gases (air, CO_2, etc.). In order to use pressurized gases, this facility is connected to the innovative fluids test loop facility by means of a CO_2 - molten salt heat exchanger. This last fa-

Figure 1. CIEMAT-PSA molten salt testing facility.

Figure 2. Thermal oil - molten salt heat exchanger.

cility comprises two parabolic-trough collectors and allow studying pressurized gases as heat transfer fluids, for further information consult Rodríguez-García (2009).

The CIEMAT-PSA molten salt testing facility, shown in figure 1 is composed by hot and cold molten salt tanks, a CO_2 - molten salt heat exchanger, a thermal oil loop, two flanged pipe sections and the electrical heat tracing. The thermal oil loop comprises a thermal oil expansion tank, a centrifugal pump, an oil heater, molten salt and oil air coolers and a thermal oil - molten salt heat exchanger. This last heat exchanger is the one considered in this work, it is described in section 2.2 and it is shown in figure 2.

2.1 Operating Modes

The multipurpose molten salt testing facility can work in four different operating modes.

- *Mode 1.* Energy from the innovative fluids test loop is used to charge the molten salt TES system by means of the CO_2 - molten salt heat exchanger.
- *Mode 2.* The molten salt is cooled down by the air cooler system.
- *Mode 3.* The TES system is charged with energy coming from the thermal oil loop by means of the thermal oil - molten salt heat exchanger.
- *Mode 4.* This mode discharges the TES system by means of the thermal oil - molten salt heat exchanger and thus heating up thermal oil.

For further details about the facility and operating modes consult Rodríguez-García and Zarza (2011) and Rodríguez-García et al. (2014).

2.2 Thermal Oil Loop Heat Exchanger

The thermal oil loop heat exchanger is composed of two counter-flow multi-pass shell-and-tube units, see figure 2. The shell-side fluid is molten salt, in particular solar salt (60 % $NaNO_3$ and 40 % KNO_3), whereas the tube-side fluid is the commercial Therminol VP-1 thermal oil, due to its high pressure (max. 15 bar). The heat exchanger nominal operating conditions in mode 3 are shown in table 1. Each unit of the heat exchanger was designed following a Tubular Exchanger Manufacturers Association (TEMA) design, in paticular a N-type front end stationary head, F-type shell and U-type rear end stationary head (NFU) design. Both units have drainage pipes at the rear end of the heat exchanger and are tilted 2° in order to facilitate their drainage. The F-type shell has two shell passes defined by a longitudinal baffle as well as two tube passes in U shape. The F-type shell is the most common and economical heat exchanger design

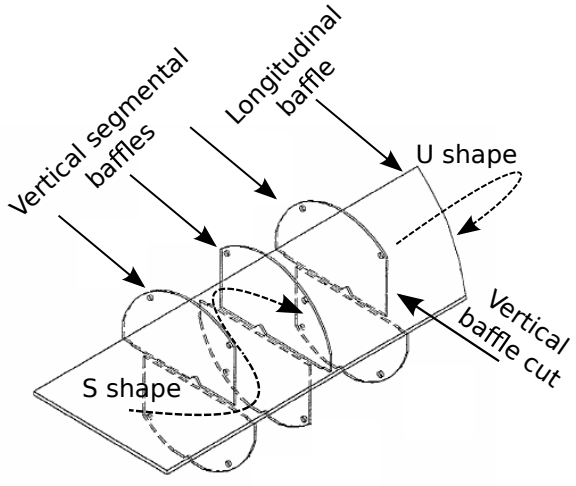

Figure 3. S-shaped and U-shaped paths along the shell side of one unit in the heat exchanger (Bonilla et al., 2015).

DOI 10.3384/ecp15118873

Table 1. Heat exchanger nominal operating conditions-mode 3

Feature	Shell side	Tube side
Fluid	Solar salt	Therminol VP-1
Inlet mass flow rate	2.08 kg/s	1.57 kg/s
Inlet pressure	2 bar	14 bar
Outlet pressure	1.6 bar	13.97 bar
Inlet temperature	290 °C	380 °C
Outlet temperature	373 °C	313 °C

used at commercial parabolic-trough solar thermal power plants (Herrmann et al., 2004). Thirty-nine vertical segmental baffles per shell pass, with vertical baffle cuts, force the shell-side fluid to follow a S-shaped path (see figure 3) in order to increase the convective heat transfer coefficient which has its highest value in cross flow. In counter flow, the tube-side fluid enters the inlet nozzle, flows along the tube bundle turning around due to the longitudinal baffle and the U-tube design, finally leaving the heat exchanger through the outlet nozzle.

3 Heat Transfer Analysis in the Heat Exchanger

Since performance losses in the heat exchanger were noticed, a heat transfer analysis considering experimental data was performed. First of all, the instrumentation installed in the facility was checked. According to the International Electrotechnical Commission (IEC) 584.3 norm, the allowable manufacturing tolerance of the K-type class 2 thermocouples is up to ±3 °C at heat exchanger nominal operating conditions (see table 1). Nevertheless, thermocouples are periodically checked against a certified reference standard and measurements are adjusted by means of polynomials functions, therefore measurement uncertainties are reduced. Both flow meters are Yokogawa GS01F06A00-01E 50 mm volumetric vortex flow meters which have an error of up to 1 % according to the manufacturer specifications.

Secondly and due to the fact that thermocouples are not installed precisely at the inlet and outlet of the heat exchanger but rather at a certain distance, thermal losses by convection and radiation in piping along the distance between the heat exchanger and thermocouples were estimated according to eq. 1.

$$\dot{Q}_{pipe,loss} = \dot{Q}_{pipe,conv} + \dot{Q}_{pipe,rad}, \tag{1}$$

$$\dot{Q}_{pipe,conv} = h_{conv} A_{pipe} (T_{pipe} - T_{amb}), \tag{2}$$

$$\dot{Q}_{pipe,rad} = h_{rad} A_{pipe} (T_{pipe} - T_{sky}). \tag{3}$$

The piping comprises an insulated metallic tube which is protected with a thin aluminum layer. The *pipe* subscript denotes the most outer part of the pipe. Nomenclature is shown in table 2. Sky temperature (T_{sky}) is assumed to be 10 °C lower than ambient temperature. The heat transfer coefficient for natural convection of air over the pipe (h_{conv}) was considered 6 W/(m^2 K) and A_{pipe} denotes the outer surface area of the piping. The radiation heat transfer coefficient (h_{rad}) is calculated according to eq. 4, where aluminum emissivity (ε_{pipe}) was assumed to be 0.09.

$$h_{rad} = \varepsilon_{pipe} \sigma \frac{T_{pipe}^4 - T_{sky}^4}{T_{pipe} - T_{sky}}. \tag{4}$$

The outer surface piping temperature (T_{pipe}) is calculated considering that thermal losses are the same as heat con-

Table 2. Nomenclature

Latin letters			
Variable	Description		Units
A	Area		[m^2]
C	Heat capacity		[J/K]
c_p	Specific heat capacity		[J/(kg K)]
d	Diameter		[m]
D	Characteristic dimension		[m]
f	Friction factor		[-]
G	Mass velocity		[kg/(m^2 s)]
h	Heat transfer coefficient		[W/(m^2 K)]
j	Chilton-Colburn j factor		[-]
K	Thermal conductivity		[W/(m K)]
l	Length		[m]
m	Mass		[kg]
$\dot{m}$	Mass flow rate		[kg/s]
n	Number of measures		[-]
Nu	Nusselt number		[-]
Pr	Prandtl number		[-]
$\dot{Q}$	Heat flow rate		[W]
Re	Reynolds number		[-]
t	Time		[s]
T	Temperature		[K]
$\dot{V}$	Volumetric flow rate		[m^3/s]
$x_1 \cdots x_4$	Calibration coefficients		[-]
y	Coefficient in ϕ		[-]
Greek letters			
Variable	Description		Units
ε	Emissivity		[-]
σ	Stefan-Boltzmann constant		[W/(m^2 K^4)]
δ	Deviation		[%]
ϕ	Viscosity correction factor		[-]
ρ	Density		[kg/m^3]
μ	Dynamic viscosity		[kg/(m s)]
Subscript	Description	Subscript	Description
amb	Ambient	*cond*	Conduction
conv	Convection	*exp*	Experimental
fluid	Fluid	*in*	Inlet
ins	Insulation	*loss*	Losses
ms	Molten salt	*oil*	Thermal oil
out	Outlet	*pipe*	Piping
rad	Radiation	*sim*	Simulated
sky	Sky	*w*	Tube wall

duction through the pipe, as it is shown in eq. 5,

$$\dot{Q}_{pipe,cond} = \dot{Q}_{pipe,conv} + \dot{Q}_{pipe,rad}, \tag{5}$$

where $\dot{Q}_{pipe,cond}$ is defined by eq. 6. It is assumed that the inner metallic tube wall temperature is the same as the fluid temperature ($T_{fluid,in}$), h_{cond} is given by eq. 7, where K_{ins} is the thermal conductivity of the insulation, l_{ins} is the insulation thickness and A_{cond} is the heat conduction area.

$$\dot{Q}_{pipe,cond} = A_{pipe} h_{cond} (T_{fluid,in} - T_{pipe}), \tag{6}$$

$$h_{cond} = \frac{K_{ins} A_{cond}}{l_{pipe} A_{pipe}}. \tag{7}$$

Therefore T_{pipe} is calculated by eq. 8,

$$T_{pipe} = \frac{h_{cond} T_{fluid,in} + h_{conv} T_{amb} + h_{rad} T_{sky}}{h_{cond} + h_{conv} + h_{rad}}. \tag{8}$$

Once thermal losses are calculated ($\dot{Q}_{pipe,loss}$), the desirable temperature, $T_{fluid,out}$ or $T_{fluid,in}$, depending on the position of the thermocouple with respect to the heat exchanger can be calculated considering eq. 9. The *in* and *out* subscripts refer to the inlet or outlet of the pipe.

$$\dot{Q}_{pipe,loss} = \dot{m}_{fluid} c_{p,fluid} (T_{fluid,out} - T_{fluid,in}). \tag{9}$$

The specific heat capacity of the fluid ($c_{p,fluid}$) can be calculated from thermodynamic properties of the particular fluid under consideration, Therminol VP-1 thermal oil (Solutia, 2008) or solar salt (Zavoico, 2001; Ferri et al., 2008) thermodynamic properties.

Once thermal losses in piping have been estimated, thermal oil ($\dot{Q}_{oil}$) and molten salt ($\dot{Q}_{ms}$) heat flow rates inside the heat exchanger should have close values in steady-state conditions, otherwise this means there are thermal losses in the heat exchanger. Heat flow rates inside the heat exchanger have been calculated considering the energy balance equation in both fluids, according to eqs. 10 and 11. The *in* and *out* subscripts refer to the heat exchanger, i.e. at the inlet or outlet of the heat exchanger.

$$\dot{Q}_{oil} = \dot{m}_{oil} c_{p,oil} (T_{oil,out} - T_{oil,in}), \tag{10}$$

$$\dot{Q}_{ms} = \dot{m}_{ms} c_{p,ms} (T_{ms,out} - T_{ms,in}). \tag{11}$$

Thermal oil and molten salt heat flow rates have been evaluated considering experimental data. The deviation between both heat flow rates has been calculated according to eq. 12.

$$\delta = 100 \frac{|\dot{Q}_{oil} - \dot{Q}_{ms}|}{\frac{1}{2}(\dot{Q}_{oil} + \dot{Q}_{ms})}. \tag{12}$$

Thermal oil and molten salt heat flow rate uncertainties inside the heat exchanger have been calculated according to the ISO/IEC Guide 98:-3:2008 Uncertainty of measurement (GUM) (International Organization of Standardization, 2008). Standard uncertainties of variables involved in eqs. 10 and 11 are given in table 3, considering volumetric flow meters for both fluids ($\dot{m} = \rho \dot{V}$). The uncertainty at a level of confidence of 95 % (coverage factor $k = 2$) of the difference between thermal oil and molten salt heat flow rates, considering mode 3 nominal operating conditions, is $U_{95}(\dot{Q}_{oil} - \dot{Q}_{ms}) = 5.70\,\%$. Figure 4 shows both heat flow rates with their uncertainty bounds in an steady-state experiment at mode 3 nominal operating conditions. It can be seen in Figure 4 that there are thermal losses in the heat exchanger. Therefore thermal losses must be estimated in order to calculate heat transfer coefficients for this heat exchanger. Section 5 presents how thermal losses have been estimated, but before that, section 4 introduces which expressions for heat transfer correlations have been considered.

Table 3. Standard uncertainties in heat flow rate variables

Var.	Standard uncertainty		Comments
	Value	Reference	
T	0.42 °C	Absolute	Periodically checked.
$\dot{V}_{oil}$	0.75 %	Relative	Manufacturer specs.
$\dot{V}_{ms}$	1.00 %	Relative	Manufacturer specs.
ρ	0.50 %	Relative	(Janz et al., 1972)
c_p	1.55 %	Relative	(Gomez et al., 2012)

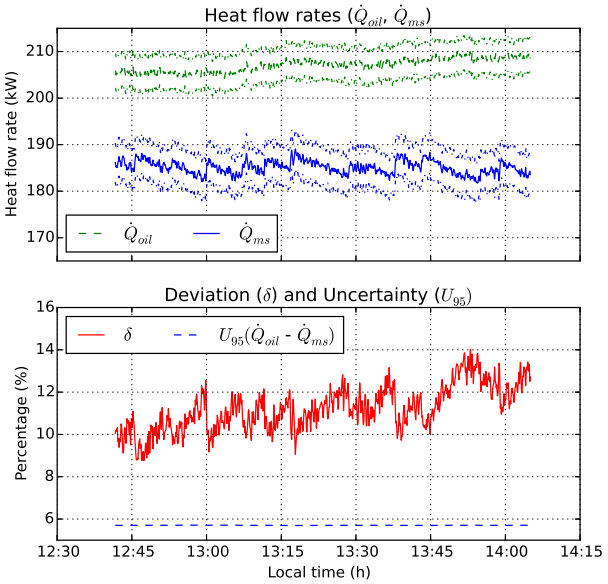

Figure 4. Steady-state case: thermal oil and molten salt heat flow rate deviation.

4 Heat Transfer Correlations

Experimental heat transfer correlations are commonly used in engineering calculations of heat transfer. In order to develop such heat transfer correlations, it is required to perform experiments to obtain experimental data and

DOI 10.3384/ecp15118873

also to correlate experimental data with appropriate expressions which involve dimensionless numbers. Those expressions are obtained from mass, energy and momentum conservation equations. A common expression to calculate the heat transfer coefficient in fully developed turbulent flow is the Chilton-Colburn j-analogy for mass (eq. 13) and heat (eq. 14).

$$j = \frac{f}{8}, \tag{13}$$

$$j = \frac{Nu}{RePr^{1/3}}, \quad Re \geq 10000, \;\; 0.7 \leq Pr \leq 160. \tag{14}$$

Eq. 15 is derived from eqs. 13 and 14, since normally the friction factor depends on the Reynolds number, $f = f(Re)$. Therefore, the Nusselts number depends on the Reynolds and Prandtl numbers, $Nu = f(Re, Pr)$, and x_1, x_2 are commonly constant coefficients.

$$Nu = x_1 Re^{x_2} Pr^{1/3}. \tag{15}$$

With the Nusselts number, the heat transfer coefficient is calculated by eq. 16, where D is the characteristic dimension.

$$h = Nu\frac{K}{D}. \tag{16}$$

Different heat transfer correlations derive from eq. 15, such as Colburn (Çengel, 2006) and Dittus and Boelter (1930) correlations. A better accuracy for estimating the heat transfer coefficient was achieved by means of the Prandtl (1910) analogy. Petukhov (1970) improved the latest, which was modified in Gnielinski (1976) as eq. 17,

$$Nu = \frac{\frac{f}{8}(Re - 1000)Pr}{1 + 12.7\sqrt{f/8}(Pr^{2/3} - 1)} \left[1 + \left(\frac{d}{l}\right)^{2/3}\right], \tag{17}$$

$$2300 \leq Re \leq 10000, \;\; 0.5 \leq Pr \leq 200.$$

Eq. 17 was derived considering fluid flow in straight ducts. Although this correlation is a good approximation for the tube side of heat exchangers, the coefficients appearing on it can be adjusted experimentally, since fluid flow path in heat exchangers is commonly complex (Taler, 2013). Eq. 18 shows Gnieliniski correlation with two coefficients that could be adjusted (x_3, x_4). Such coefficients have different values in the Prandtl analogy, Petukhov, and Gnielinski correlations, therefore they are suitable coefficients to be tuned.

$$Nu = \frac{\frac{f}{8}(Re - x_3)Pr}{1 + x_4\sqrt{f/8}(Pr^{2/3} - 1)} \left[1 + \left(\frac{d}{l}\right)^{2/3}\right]. \tag{18}$$

An equivalent expression to eq. 16, and commonly used to calculate the ideal cross-flow heat transfer coefficient in the shell side of heat exchangers, is given by eq. 19,

$$h = \frac{jc_pG}{Pr^{2/3}}. \tag{19}$$

This expression is used in the Bell-Delaware method, among others. The ideal heat transfer coefficient is modified for the presence of streams by means of corrections factors, such as corrections factors for baffle cut and spacing, baffle leakage, bundle bypass flow, variable baffle spacing in the inlet and outlet sections, adverse temperature gradient buildup in laminar flow, etc. Check the Taborek implementation of the Bell-Delaware method (Thulukkanam, 2013) for further information.

The mass velocity (G) takes into account the tube bank inside the shell. The ideal Colburn j factor for the shell side is expressed as eq. 20,

$$j = x_1 Re^{x_2}, \tag{20}$$

where x_1 and x_2 are constant values within an interval of Reynolds numbers. The Reynolds number is usually calculated by eq. 21,

$$Re = \frac{GD}{\mu}. \tag{21}$$

There are other versions of eqs. 17 and 19 which incorporate the viscosity correction factor (ϕ), eq. 22, in order to take into account the viscosity gradient at the wall (μ_w) versus the viscosity at the bulk mean temperature (μ) of the fluid. The y coefficient usually depends on the ratio between viscosities (Wichterle, 1990), authors propose different values in the literature.

$$\phi = \left(\frac{\mu}{\mu_w}\right)^y. \tag{22}$$

5 Calibration of Thermal Losses

Eq. 11 has been modified in order to account for thermal losses from the shell-side fluid to the ambient and eq. 23 has been obtained.

$$\dot{Q}_{ms} = \dot{m}_{ms}c_{p,ms}(T_{ms,out} - T_{ms,in}) + Q_{loss}. \tag{23}$$

Convective heat losses have been roughly approximated considering the shell-side (T_{ms}) and ambient (T_{amb}) temperatures in the Newton's law of cooling, as shown in eq. 24. The shell-side temperature is the arithmetic mean temperature between the inlet and outlet molten salt temperatures in the heat exchanger. A_{loss} is the outer surface area of the whole heat exchanger.

$$\dot{Q}_{loss} = h_{loss}A_{loss}(T_{ms} - T_{amb}). \tag{24}$$

The heat transfer coefficient (h_{loss}) has been defined considering eq. 19. The characteristic dimension is the inner equivalent hydraulic diameter of the shell side, x_1 and x_2 from eq. 20 have been calibrated considering experimental data. Three different experimental data sets in steady state with different flow conditions have been used in the calibration process, where ($\dot{m}_{oil}$,$\dot{m}_{ms}$) = [(1.4 kg/s, 2.0 kg/s), (1.4 kg/s, 3.2 kg/s), (1.95 kg/s, 2.0 kg/s)].

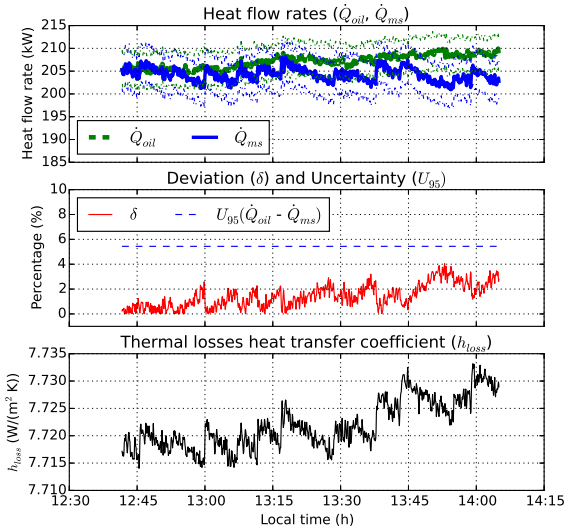

Figure 5. Steady-state case with thermal losses: thermal oil and molten salt heat flow rate deviation.

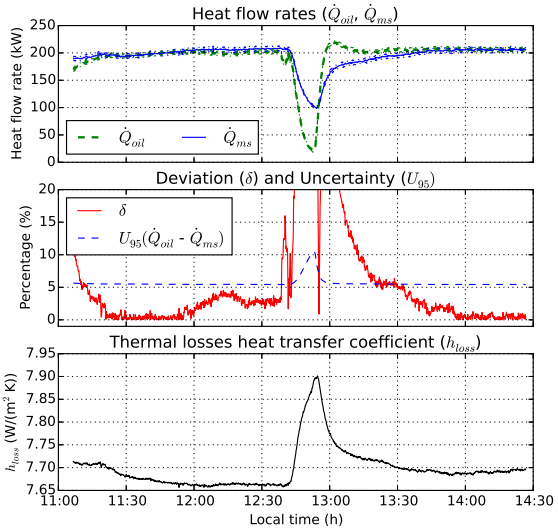

Figure 6. Cloud disturbances case: thermal oil and molten salt heat flow rate deviation.

For the calibration of the x_1 and x_2 parameters, the JModelica.org tool (Åkesson et al., 2010) has been used. The optimization problem was formulated according to eq. 25, where n is the number of measures and t_i represents a time instant.

$$\min_{x_1,x_2} \sum_{i=0}^{n} (\dot{Q}_{oil}(t_i) - \dot{Q}_{ms}(t_i, x_1, x_2))^2. \tag{25}$$

The Nelder-Mead simplex optimization algorithm (Conn et al., 2009) performed the calibration process, the three considered experimental data sets are equally distributed, therefore each of them has $n/3$ measures. As a result of the calibration, the following values were obtained: $x_1 = 1.1858$ and $x_2 = -0.9545$. Therefore, eq. 20 is modified as eq. 26,

$$j_{loss} = 1.1858 Re_{loss}^{-0.9545}. \tag{26}$$

Heat flow rates from experimental data presented in section 3 are evaluated in figure 5, but in this case considering thermal losses according to eqs. 23, 24, 19 and 26. It can be seen that there is a good agreement between both heat flow rates since the difference is lower than the uncertainty.

Figure 6 shows heat flow rates in an experiment replicating cloud disturbances in the solar field, since the inlet thermal oil temperature was reduced and then set it back to its original value. Figure 7 shows another experiment where steps in thermal oil and molten salt mass flow rates were applied. It can be seen in both figures that in steady state the deviation between both heat flow rates is lower than the uncertainty. It can be also inferred from the three experiments that the thermal losses heat transfer coefficient does not vary much and a constant value of 7.725 W/(m^2 K) could be assumed.

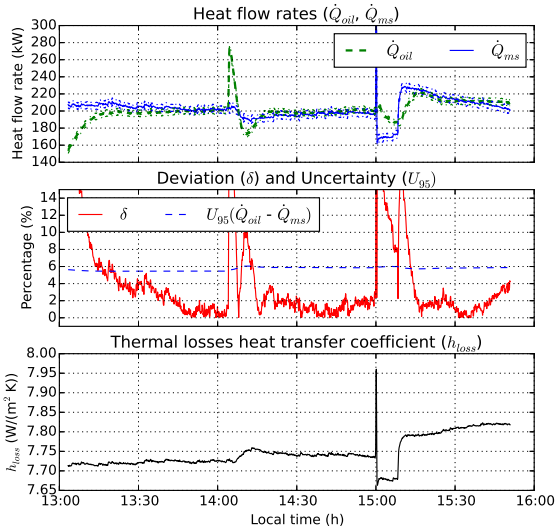

Figure 7. Mass flow rate steps case: thermal oil and molten salt heat flow rate deviation.

6 Heat Transfer Calibration

A simplified dynamic heat exchanger model has been considered in order to calibrate heat transfer correlations for the tube side as well as for the shell side. This dynamic model was presented in Correa and Marchetti (1987). It is a dynamic distributed parameter model, where each cell or Control Volume (CV) is a small lumped parameter counter-flow heat exchanger model. This model considers the thermal capacitance of the tube bundle but it neglects that of the shell metallic parts and there is neither pressure loss at the shell side nor at the tube side, thus inlet and outlet mass flow rates are equal. Eqs. 27 and 28 represent the energy balance for the tube side and the shell side respectively in each cell of the model.

DOI 10.3384/ecp15118873

$$C_{oil}\frac{dT_{oil,out}}{dt} = \dot{m}_{oil}c_{p,oil}(T_{oil,in} - T_{oil,out}) + \dot{Q}_{oil}, \quad (27)$$

$$C_{ms}\frac{dT_{ms,out}}{dt} = \dot{m}_{ms}c_{p,ms}(T_{ms,in} - T_{ms,out}) + \dot{Q}_{ms}, \quad (28)$$

where heat capacities are defined by eqs. 29 and 30,

$$C_{oil} = m_{oil}c_{p,oil} + \frac{1}{2}m_w c_{p,w}, \quad (29)$$

$$C_{ms} = m_{ms}c_{p,ms} + \frac{1}{2}m_w c_{p,w}, \quad (30)$$

and heat flow rates by eqs. 31 and 32,

$$\dot{Q}_{oil} = hA_w(T_{ms,out} - T_{oil,out}), \quad (31)$$

$$\dot{Q}_{ms} = hA_w(T_{oil,out} - T_{ms,out}) - \dot{Q}_{loss}. \quad (32)$$

The overall heat transfer coefficient (h) can be calculated by eq. 33,

$$\frac{1}{h} = \frac{1}{h_{oil}} + \frac{1}{h_{ms}}, \quad (33)$$

and thermal losses by eq. 24. Thermal losses have been already calibrated in section 5 and are included in the model by means of eqs. 24, 19 and 26.

Several heat transfer correlations have been implemented in the model and compared against experimental data. In the shell side: Gaddis and Gnielinski (VDI, 2010), the Bell-Delaware method (Thulukkanam, 2013) and a correlation proposed in Serth (2007) which is a curve fit from data provided in Kraus et al. (2002), whereas in the tube side: Gnielinski (1976), Dittus and Boelter (1930) and Hausen (1943) correlations have been also tested.

However, simulation results did not agree with experimental data. This is because there are performance losses in this heat exchanger (Bonilla et al., 2015). The most common causes for deterioration in performance of F-shell heat exchangers are thermal leakage or physical leakage due to the longitudinal baffle (Mukherjee, 2004) together with fouling, corrosion, design errors and fabrication issues. Additionally, two potential issues were identified with this heat exchanger, as presented in Rodríguez-García et al. (2014). One of them is the bypass of molten salt through the drainage channels and the other one is the nitrogen accumulation inside the shell due to the heat exchanger tilt angle. Further investigation is necessary, but in order to have an available dynamic model of the heat exchanger, heat transfer correlations have been calibrated with experimental data.

The shell-side heat transfer coefficient (h_{ms}) is defined considering eq. 19. The characteristic dimension is the outer tube diameter of the tubes in the tube bundle. The tube-side heat transfer coefficient (h_{oil}) is defined considering eq. 18, where the characteristic dimension is the inner tube diameter and the friction factor has been calculated considering the Filonenko (1954) correlation, eq. 34,

$$f_w = (1.82\log Re_{oil} - 1.64)^{-2}. \quad (34)$$

The remaining coefficients, x_1, x_2 (from eq. 20), x_3 and x_4 (from eq. 18) have been calibrated considering experimental data.

In Correa and Marchetti (1987), the number of cells was the number of baffles plus one multiply by the number of tube passes, however in our case that could make a total of 160 CVs, since the studied heat exchanger has 39 baffles per unit with two passes per unit. In order to reduce the time required for the calibration, the number of cells has been set to 80 CVs. Comparing simulation results, it can be stated that the maximum difference in outlet molten salt and thermal oil temperatures between the 160-CV and 80-CV models is lower than 1 °C.

The JModelica.org tool has been also used to perform the calibration process with the same experimental data sets and algorithm than for the calibration of heat losses. The optimization problem was formulated according to eq. 35.

$$\min_{x_1\cdots x_4}\sum_{i=0}^{n}((T_{oil,out,exp}(t_i) - T_{oil,out,sim}(t_i,x_1,x_2))^2 + (T_{ms,out,exp}(t_i) - T_{ms,out,sim}(t_i,x_3,x_4))^2). \quad (35)$$

As a result of the calibration, the following values were obtained: $x_1 = 3.2470$, $x_2 = -1.1077$, $x_3 = 1792$ and $x_4 = 29.93$. Therefore, eqs. 20 and 18 are modified as eqs. 36 and 37,

$$j_{ms} = 3.2470 Re_{ms}^{-1.1077}, \quad (36)$$

$$Nu_{oil} = \frac{\frac{f_w}{8}(Re_{oil} - 1792)Pr_{oil}}{1 + 29.93\sqrt{f_w/8}(Pr_{oil}^{2/3} - 1)}\left[1 + \left(\frac{d_w}{l_w}\right)^{2/3}\right]. \quad (37)$$

The three cases, previously analyzed in section 5, are also presented in this section in terms of temperature.

Figure 8 shows, for the steady-state case, the experimental inlet, experimental outlet and simulated outlet molten salt and thermal oil temperatures together with temperature differences between experimental and simulated outlet temperatures for both fluids. It can be seen that there is a good agreement, where the maximum difference between experimental and simulated outlet temperature for both fluid is lower than 3 °C. Figure 9 shows inlet mass flow rates and heat transfer coefficients for both fluids. Same information is shown in Figures 10 and 11, but in this case for the experiment which replicates cloud disturbances. The experimental and simulated outlet temperature differences for both fluids are lower than 5 °C in general, only when the inlet thermal oil temperature is decreased (12:40 in Figure 10), the dynamic model reacts much faster than the real system in terms of thermal oil outlet temperature. This must be further studied, it might be related to unmodeled dynamics, such as the inlet and outlet channels in the tube side of each unit in the heat exchanger, approximate heat capacities or to issues in the thermocouple. Finally, same information is also shown for the case of mass flow rate

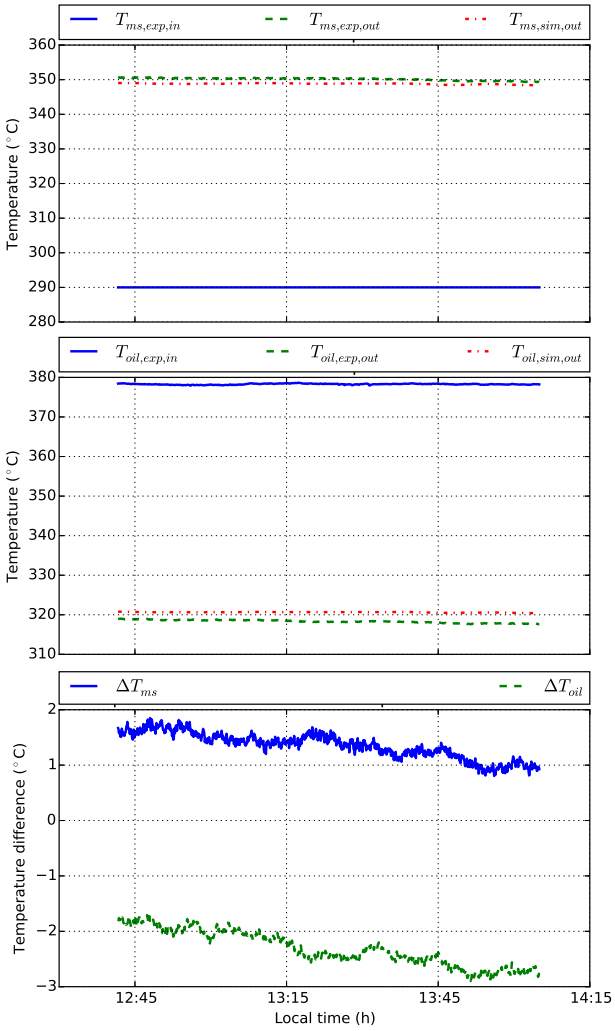

Figure 8. Steady-state case: temperatures.

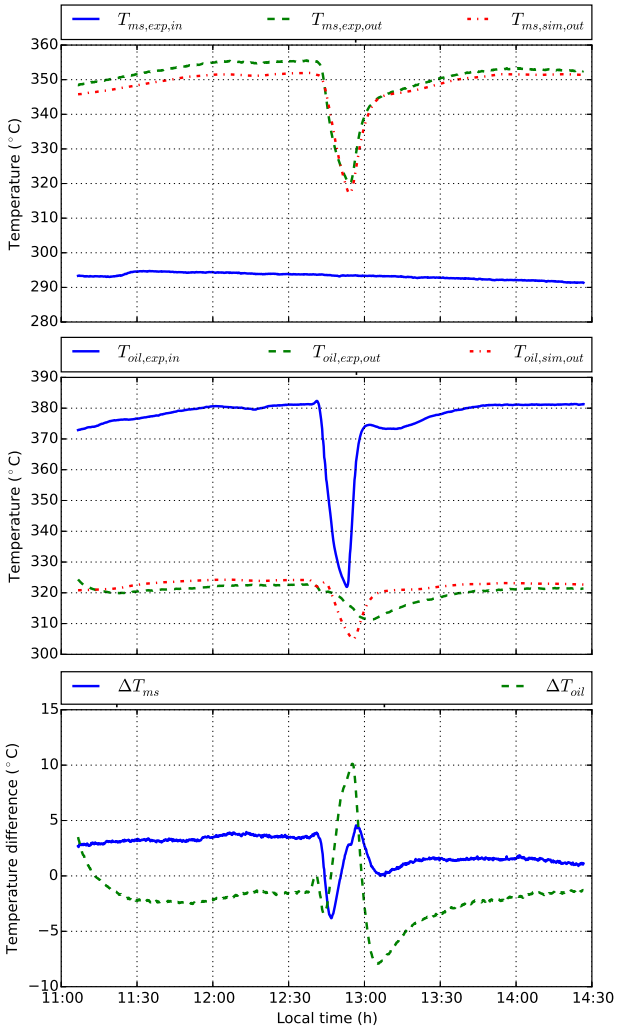

Figure 10. Cloud disturbances case: temperatures.

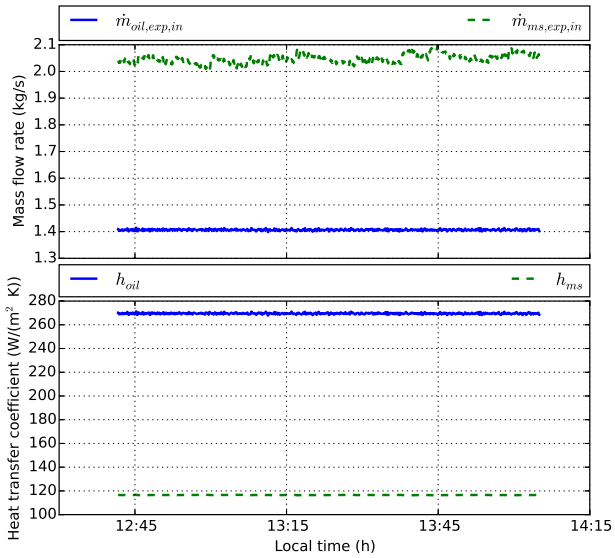

Figure 9. Steady-state case: mass flow rates and heat transfer coefficients.

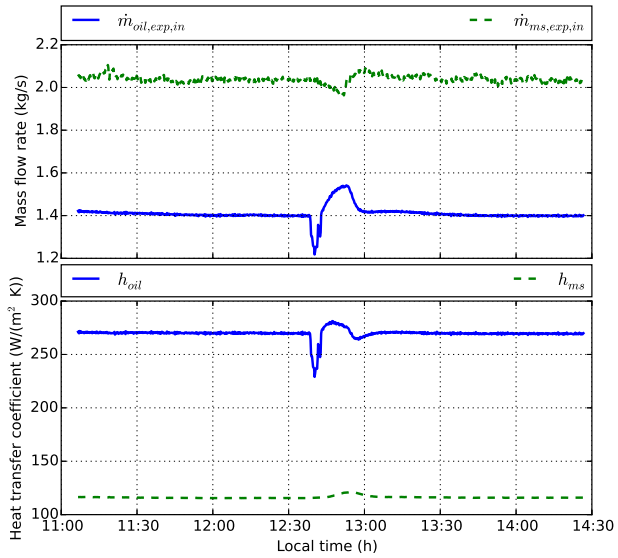

Figure 11. Cloud disturbances case: mass flow rates and heat transfer coefficients.

DOI 10.3384/ecp15118873

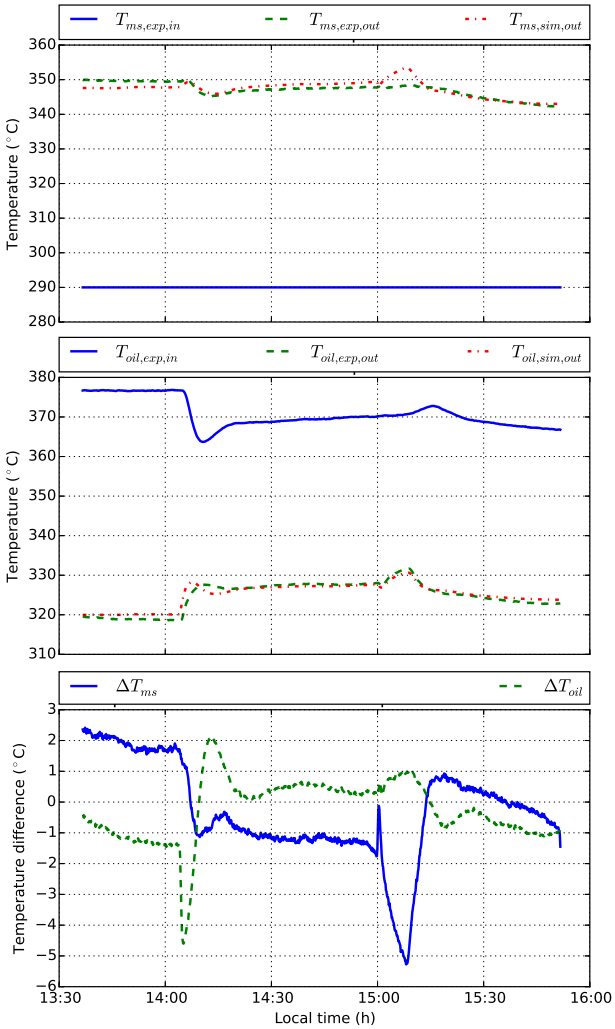

Figure 12. Mass flow rate steps case: temperatures.

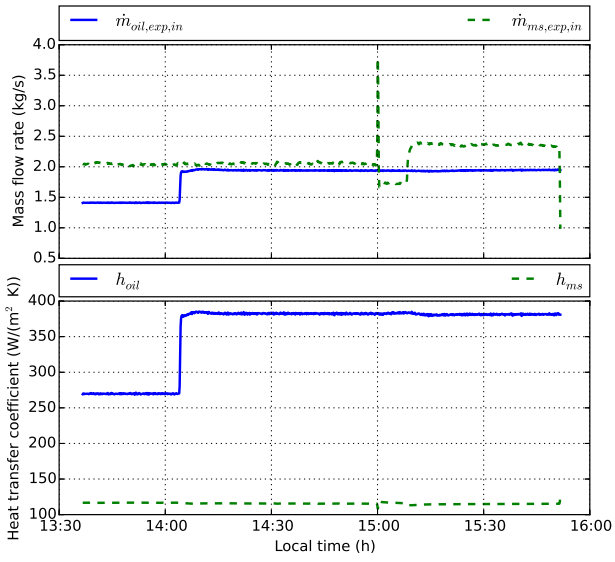

Figure 13. Mass flow rate steps case: mass flow rates and heat transfer coefficients.

steps in both fluids, as shown in Figures 12 and 13, where the experimental and simulated outlet temperature differences for both fluid are lower than 5.5 °C. There are two issues that must be studied in this case. The first one is the dynamic model response to the thermal oil mass flow rate step (14:05 in Figure 12), again the dynamic model is faster than the real system. And the second one is the increase in molten salt outlet temperature (15:00 in Figure 12), when the molten salt mass flow rate is decreased (see Figure 13). This behavior does not occur in the real system.

7 Conclusions and Ongoing Work

This paper has shown a methodology to estimate thermal losses and heat transfer correlations using Modelica and JModelica.org rather than final results, since further experimental campaigns in the facility are required in order to calibrate, if necessary, and validate the developed correlations in a wider range of operating conditions. Nevertheless, experimental data has been used to fit parameters in commonly used heat transfer correlation expressions and simulation results have been compared against experimental data with a good agreement.

Ongoing work includes integrating the calibrated correlations in a more detailed model of the heat exchanger (Bonilla et al., 2015), improving the detailed model considering a more detailed shell model as well as tube bundle model applying the cell method but particularized for a F-shell heat exchanger, as demonstrated in Zaversky et al. (2014), studying the causes of the performance losses in the heat exchanger and performing additional experimental campaigns to validate the results.

References

J. Åkesson, K. E. Årzén, M. Gäfvert, T. Bergdahl, and H. Tummescheit. Modeling and optimization with Optimica and JModelica.org-Languages and tools for solving large-scale dynamic optimization problems. *Computers and Chemical Engineering*, 34(11):1737–1749, 2010. ISSN 00981354. doi:10.1016/j.compchemeng.2009.11.011.

J. Bonilla, M.-M. Rodríguez-García, L. Roca, and L. Valenzuela. Object-Oriented Modeling of a Multi-Pass Shell-and-Tube Heat Exchanger and its Application to Performance Evaluation. In *1st Conference on Modelling, Identification and Control of Nonlinear Systems (MICNON)*, pages 107 – 112, Saint-Petersburg, Russia, 2015.

Y. A. Çengel. *Heat Transfer: A Practical Approach (3rd edition)*. McGraw-Hill series in mechanical engineering. McGraw-Hill, 2006. ISBN 9780072458930.

A. Conn, K. Scheinberg, and L. Vicente. *Introduction to Derivative-Free Optimization*. Society for Industrial and Applied Mathematics, 2009. doi:10.1137/1.9780898718768.

D. J. Correa and J. L. Marchetti. Dynamic Simulation of Shell-and-Tube Heat Exchangers. *Heat Transfer Engineering*, 8 (1):50 – 59, 1987. doi:10.1080/01457638708962787.

F. W. Dittus and L. M. K. Boelter. Heat transfer in automobile radiators of the tubular type. *University of California Publications in Engineering*, 2(1):443–461, 1930. ISSN 07351933. doi:10.1016/0735-1933(85)90003-X.

R. Ferri, A. Cammi, and D. Mazzei. Molten salt mixture properties in RELAP5 code for thermodynamic solar applications. *International Journal of Thermal Sciences*, 47(12):1676–1687, December 2008. ISSN 12900729. doi:10.1016/j.ijthermalsci.2008.01.007.

G. K. Filonenko. Hydraulic drag in pipes. *Teploenergetika*, 1 (4):40 – 44, 1954.

V. Gnielinski. New equations for heat and mass transfer in turbulent pipe flow and channel flow. *International Chemical Engineering*, 2(16):359–368, 1976.

J. C. Gomez, G. C. Glatzmaier, and M. Mehos. Heat Capacity Uncertainty Calculation for the Eutectic Mixture of Biphenyl / Diphenyl Ether Used As Heat Transfer Fluid. *SolarPaces Conference*, (September), 2012.

H. Hausen. Darstellung des Wärmeüberganges in Rohren durch verallgemeinerte Potenzbeziehyngen. *VDI - Verfahrenstechnik*, 4:91–98, 1943.

U. Herrmann and D. W. Kearney. Survey of Thermal Energy Storage for Parabolic Trough Power Plants. *Journal of Solar Energy Engineering*, 124(2):145, 2002. ISSN 01996231. doi:10.1115/1.1467601.

U. Herrmann, B. Kelly, and H. Price. Two-tank molten salt storage for parabolic trough solar power plants. *Energy*, 29(5-6):883–893, April 2004. ISSN 03605442. doi:10.1016/S0360-5442(03)00193-2.

International Organization of Standardization. ISO/IEC Guide 98-3:2008 Uncertainty of measurement – Part 3: Guide to the expression of uncertainty in measurement (GUM:1995). Technical report, Switzerland, 2008.

G. J. Janz, U. Krebs, H. F. Siegenthaler, and R. P. T. Tomkins. Molten Salts: Volume 3 Nitrates, Nitrites, and Mixtures: Electrical Conductance, Density, Viscosity, and Surface Tension Data, 1972. ISSN 00472689.

A. D. Kraus, A. Aziz, and J. Welty. *Extended Surface Heat Transfer*. Wiley, 2002. ISBN 9780471436638.

R. Mukherjee. Does Your Application Call for an F-Shell Heat Exchanger? *CEP magazine*, (April):40–45, 2004.

B. S. Petukhov. Heat Transfer and Friction in Turbulent Pipe Flow with Variable Physical Properties. *Advances in Heat Transfer*, 6(C):504–564, 1970. ISSN 00652717. doi:10.1016/S0065-2717(08)70153-9.

L. Prandtl. Eine Beziehung zwischen Warmeaustausch und Stromungswiderstand der Flussigkeiten. *Physik Z*, 11:1072 – 1075, 1910.

M.-M. Rodríguez-García. First Experimental Results of a PTC Facility Using Gas as the Heat Transfer Fluid. In *15th SolarPACES Conference*, Berlin, Germany, 2009.

M.-M. Rodríguez-García and E. Zarza. Design and Construction of an Experimental Molten Salt Test Loop. In *17thSolarPACES Conference*, Granada, Spain, 2011.

M.-M. Rodríguez-García, M. Herrador-Moreno, and E. Zarza Moya. Lessons learnt during the design, construction and start-up phase of a molten salt testing facility. *Applied Thermal Engineering*, 62(2):520–528, January 2014. ISSN 13594311. doi:10.1016/j.applthermaleng.2013.09.040.

R. W. Serth. *Process Heat Transfer: Principles and Applications*. Elsevier Science, 2007. ISBN 9780123735881.

Solutia. Therminol VP-1 heat transfer fluid - Vapour and Liquid phases. Technical bulletin 7239115C, 2008.

D. Taler. Experimental determination of correlations for average heat transfer coefficients in heat exchangers on both fluid sides. *Heat and Mass Transfer/Waerme- und Stoffuebertragung*, 49(8):1125–1139, 2013. ISSN 14321181. doi:10.1007/s00231-013-1148-5.

K. Thulukkanam. Shell and Tube Heat Exchanger Design. In *Heat Exchanger Design Handbook, Second Edition*, Dekker Mechanical Engineering, pages 237–336. CRC Press, 2013. ISBN 978-1-4398-4212-6. doi:doi:10.1201/b14877-6.

VDI. *VDI Heat Atlas*. Springer, 2nd edition, 2010. ISBN 9783540778769.

K. Wichterle. A theoretical viscosity correction factor for heat transfer and friction in pipe flow. *Chemical Engineering Science*, 45(5):1343 – 1347, 1990. ISSN 00092509. doi:10.1016/0009-2509(91)85083-A.

F. Zaversky, M. M. Rodríguez-García, J. García-Barberena, M. Sánchez, and D. Astrain. Transient behavior of an active indirect two-tank thermal energy storage system during changes in operating mode - An application of an experimentally validated numerical model. *Energy Procedia*, 49:1078–1087, 2013. ISSN 18766102. doi:10.1016/j.egypro.2014.03.117.

F. Zaversky, M. Sánchez, and D. Astrain. Object-oriented modeling for the transient response simulation of multipass shell-and-tube heat exchangers as applied in active indirect thermal energy storage systems for concentrated solar power. *Energy*, 65:647–664, February 2014. ISSN 03605442. doi:10.1016/j.energy.2013.11.070.

A. B. Zavoico. Solar Power Tower - Design Basis Document. Technical Report SAND2001-2100, Sandia National Laboratories, Albuquerque, USA, 2001.

Acknowledgments

This research has been funded by the EU 7th Framework Programme (Theme Energy 2012.2.5.2) under grant agreement 308912 - HYSOL project - Innovative Configuration of a Fully Renewable Hybrid CSP Plant and the Spanish Ministry of Economy and Competitiveness through ERDF and PLAN E funds (C.N. SolarNOVA ICT-CEPU 2009-02).